

Förster resonance energy transfer with transient coherent effects: Supporting Information

Maximilian Meyer-Mölleringhof,^{1,*} Pablo Martinez-Azcona,^{1,2,†} Aurélia Chenu,^{1,‡} and Tomáš Mančal^{2,§}

¹*Department of Physics and Materials Science, University of Luxembourg, L-1511 Luxembourg*

²*Faculty of Mathematics and Physics, Charles University,
Ke Karlovu 5, CZ-121 16 Prague 2, Czech Republic*

(Dated: February 19, 2026)

In the Supplementary Information we provide further details on the computations of the main text. Particularly, we provide: a detailed form of the gFT master equation with each of its terms, details on the correlation and lineshape functions used, details on the numerical integration of the integro-differential equation, an analysis on the effects of the phase in the initial coherence and an extensive comparison of gFT with HEOM and non-equilibrium Förster for different values of ΔE .

CONTENTS

A. Master Equation Terms	1
1. Initial Term	2
2. Hamiltonian and Dephasing Terms	2
3. Memory kernel	3
4. Full equation of motion for the RDM	4
5. Relaxation Rates	4
B. Bath correlation functions and lineshape functions	4
C. Numerical integration of integro-differential equation	5
D. The Influence of Time Non-Local Effects	5
E. Comparison with Numerically Exact Propagation	6
1. Molecules on resonance $\Delta E = 0$	6
2. Intermediate energy difference $\Delta E = 50$	9
3. Large energy difference $\Delta E = 300$	11
References	12

A: Master Equation Terms

Here, we present the derivation of the approximate equation of motion for the reduced density matrix, Eq. (2), of the main text. The general form consists of an initial term $\hat{I}(t)$, the Hamiltonian term, and an integral term with a memory kernel. The form of these terms can be derived exactly from the Liouville-von Neumann equation for the system and bath state $\hat{W}(t)$

$$\frac{\partial}{\partial t} \hat{W}(t) = -\frac{i}{\hbar} [\hat{H}, \hat{W}(t)]. \quad (\text{A1})$$

The Hamiltonian is split into the unperturbed part, \hat{H}_0 , and the interaction part, \hat{V} . In the Förster case, the operator \hat{V} does not depend on the bath degrees of freedom. Using the interaction picture with respect to \hat{H}_0 , we obtain

$$\frac{\partial}{\partial t} \hat{W}^{(I)}(t) = -\frac{i}{\hbar} [\hat{V}(t), \hat{W}^{(I)}(t)], \quad (\text{A2})$$

* These authors contributed equally to this work

† These authors contributed equally to this work. Current affiliation: Walther-Meißner-Institut/ Technical University of Munich, 85748 Garching, Germany

‡ aurelia.chenu@uni.lu

§ tomas.mancal@matfyz.cuni.cz

where $\hat{W}^{(I)}(t) = \hat{U}_0^\dagger(t)\hat{W}(t)\hat{U}_0(t)$ and $\hat{V}(t) = \hat{U}_0^\dagger(t)\hat{V}\hat{U}_0(t)$. By integrating Eq. (A2) and reinserting the result into the same equation, we obtain

$$\frac{\partial}{\partial t}\hat{W}^{(I)}(t) = -\frac{i}{\hbar}[\hat{V}(t), \hat{W}^{(I)}(0)] - \frac{1}{\hbar^2} \int_0^t d\tau [\hat{V}(t), [\hat{V}(\tau), \hat{W}^{(I)}(\tau)]]. \quad (\text{A3})$$

Returning to the Schrödinger picture, $\frac{\partial}{\partial t}\hat{W}(t) = -\frac{i}{\hbar}[\hat{H}_0, \hat{W}(t)] + \hat{U}_0(t)\frac{\partial\hat{W}^{(I)}(t)}{\partial t}U_0^\dagger(t)$, and performing a substitution $\tau' = t - \tau$ we obtain

$$\frac{\partial}{\partial t}\hat{W}(t) = -\frac{i}{\hbar}[\hat{V}, \hat{U}_0(t)\hat{W}(0)\hat{U}_0^\dagger(t)] - \frac{i}{\hbar}[\hat{H}_0, \hat{W}(t)] - \frac{1}{\hbar^2} \int_0^t d\tau' [\hat{V}, \hat{U}_0(\tau')[\hat{V}, \hat{W}(t - \tau')]\hat{U}_0^\dagger(\tau'). \quad (\text{A4})$$

This is Eq. (1) in the main text.

By using a formally exact factorization of the density matrix elements

$$\hat{W}(t) = \sum_{a,b} \text{tr}_B\{\hat{W}_{ab}(t)\} |a\rangle\langle b| \frac{\hat{W}_{ab}(t)}{\text{tr}_B\{\hat{W}_{ab}(t)\}} = \sum_{a,b} \rho_{ab}(t) |a\rangle\langle b| \hat{w}_{ab}(t), \quad (\text{A5})$$

and assuming zero-order approximation for the bath relative operators

$$\hat{w}_{ab}(t) = \frac{\hat{u}_a(t)\hat{w}_{eq}\hat{u}_b^\dagger(t)}{\text{tr}_B\{\hat{u}_a(t)\hat{w}_{eq}\hat{u}_b^\dagger(t)\}} = \frac{\hat{u}_a(t)\hat{w}_{eq}\hat{u}_b^\dagger(t)}{G_{ab}(t)}, \quad (\text{A6})$$

we can formally trace over the bath degrees of freedom in Eq. (A4) and obtain the term of the reduced density matrix master equation, as shown below.

1. Initial Term

For the initial condition term (the first term on the r.h.s. of Eq. (2)), we obtain

$$\hat{I}(t) = -\frac{i}{\hbar} \text{tr}_B\{[\hat{V}, U_0(t)\rho(0)\hat{w}_{eq}U_0^\dagger(t)]\} = -\frac{i}{\hbar} \sum_{ab} [\hat{V}, |a\rangle\langle a|] D_{ab}(t) \rho_{ab}(0) \langle b| \quad (\text{A7})$$

$$= -\frac{i}{\hbar} \sum_{ab} \rho_{ab}(0) D_{ab}(t) \sum_c (J_{ca} |c\rangle\langle b| - J_{bc} |a\rangle\langle c|), \quad (\text{A8})$$

where we introduced

$$\begin{aligned} D_{ab}(t) &= \text{tr}_B\{\hat{u}_a(t)\hat{w}_{eq}\hat{u}_b^\dagger(t)\} e^{-i\omega_{ab}t} \\ &= e^{-g_{aa}(t) - g_{bb}^*(t) + 2\text{Re}[g_{ab}(t)]} e^{-i\omega_{ab}t} \end{aligned} \quad (\text{A9})$$

and used the cumulant expansion to evaluate it in the second line. The lineshape function $g(t)$ is detailed in Eq. (B3). The initial term elements $I_{ab}(t)$ thus read

$$I_{ab}(t) = \langle a|\hat{I}(t)|b\rangle = -\frac{i}{\hbar} (J_{ac}D_{cb}(t)\rho_{cb}(0) - D_{ac}(t)\rho_{ac}(0)J_{cb}). \quad (\text{A10})$$

2. Hamiltonian and Dephasing Terms

For the Hamiltonian term of Eq. (2) in the main text (the second term on the r.h.s.), we obtain

$$\mathcal{L}(t)\hat{\rho}(t) = \frac{1}{\hbar}[H_S, \rho(t)] - i\mathcal{D}(t)\hat{\rho}(t) = \hat{\Omega}(t) \circ \hat{\rho}(t). \quad (\text{A11})$$

The second term represents the dephasing due to the bath evolution,

$$\mathcal{D}(t)\hat{\rho}(t) = -\frac{i}{\hbar} \sum_{ab} (x_{\underline{a}b}(t) - x_{a\underline{b}}(t)) \rho_{ab}(t) |a\rangle\langle b|, \quad (\text{A12})$$

which depends on the shift of the environment due to the electronic excitation, captured by the function

$$x_{\underline{a}b}(t) \equiv \text{Tr}_B \left(\hat{X}_a \hat{w}_{ab}(t) \right). \quad (\text{A13})$$

In this notation, we highlight the state that experiences the electronic transition with the underlined subscript—so $x_{\underline{a}b}(t) = \text{Tr}_B (\hat{w}_{ab}(t) \hat{X}_b) = x_{\underline{b}a}^*(t)$.

We need to evaluate $\text{Tr}_B \{ \hat{u}_b^\dagger(t) \hat{X}_a \hat{u}_a(t) w_{eq} \} = -i(\dot{g}_{aa}(t) - \dot{g}_{ab}^*(t)) e^{-g_{aa}(t) - g_{bb}^*(t) + 2\text{Re}g_{ab}(t)}$ which gives, after dividing by the normalization $G_{ab}(t)$

$$x_{\underline{a}b}(t) = -i\dot{g}_{aa}(t) + i\dot{g}_{ab}^*(t), \quad (\text{A14})$$

and

$$x_{a\underline{b}}(t) = i\dot{g}_{bb}^*(t) - i\dot{g}_{ab}(t). \quad (\text{A15})$$

In the equation of motion, these terms appear as a difference, cf. Eq. (A11), which can be expressed by the frequency

$$\begin{aligned} \Omega_{ab}(t) &\equiv \omega_{ab} + \text{Tr}_B(\hat{X}_a \hat{w}_{ab}(t)) - \text{Tr}_B(\hat{w}_{ab}(t) \hat{X}_b) \\ &= \omega_{ab} + x_{\underline{a}b}(t) - x_{a\underline{b}}(t), \end{aligned} \quad (\text{A16})$$

written using the lineshape function $g(t)$ in Eq. (8) of the main text. Note that, by construction, $\Omega_{aa}(t) = 0$.

3. Memory kernel

The integral kernel of the third term on the r.h.s. of Eq. (2) leads to the superoperator

$$\mathcal{M}(t, \tau) \rho(t-\tau) = \sum_{ab} [\hat{V}, \text{tr}_B \left\{ \hat{U}_0(\tau) [\hat{V}, |a\rangle\langle b|] \hat{w}_{ab}(t-\tau) \hat{U}_0^\dagger(\tau) \right\}] \rho_{ab}(t-\tau) |a\rangle\langle b|. \quad (\text{A17})$$

To express this equation, we define the bath evolution correlators

$$f_{ab}^{a'b'}(t, \tau) \equiv \text{tr}_B \{ \hat{u}_{a'}(\tau) \hat{w}_{ab}(t-\tau) \hat{u}_b^\dagger(\tau) \}, \quad (\text{A18})$$

where the box notation is inspired from the Feynman double-sided diagram, as illustrated in Fig. 1. Note that this function enters in the dynamics with only one interaction, i.e. either $a' = a$ or $b = b'$. The explicit form for this function is given in Eq. (10) of the main text.

We further introduce the system operators $\hat{V}_{\underline{a}b}(t, \tau)$ and $\hat{V}_{a\underline{b}}(t, \tau)$ that describe the free evolution of the relative bath state \hat{w}_{ab} from time $t-\tau$ to t after one interaction V , that is, allowing for one electronic transition on the state which index is underlined. Namely,

$$\begin{aligned} \hat{V}_{\underline{a}b}(t, \tau) &= \text{tr}_B \{ \hat{U}_0(\tau) \hat{V} |a\rangle\langle b| \hat{w}_{ab}(t-\tau) \langle b| \hat{U}_0^\dagger(\tau) \} \\ &= \sum_{a'} J_{a'a} e^{-\frac{i}{\hbar} \varepsilon_{a'} \tau} f_{ab}^{a'b}(t, \tau) e^{\frac{i}{\hbar} \varepsilon_b \tau} |a'\rangle\langle b|, \end{aligned} \quad (\text{A19})$$

$$\begin{aligned} \hat{V}_{a\underline{b}}(t, \tau) &= \text{tr}_B \{ U_0(\tau) |a\rangle\langle b| w_{ab}(t-\tau) \langle b| \hat{V} U_0^\dagger(\tau) \} \\ &= \sum_{b'} J_{ab'} e^{-\frac{i}{\hbar} \varepsilon_a \tau} f_{ab}^{ab'}(t, \tau) e^{\frac{i}{\hbar} \varepsilon_{b'} \tau} |a\rangle\langle b'|. \end{aligned} \quad (\text{A20})$$

The memory kernel has four contributions corresponding to the two nested commutators

$$\begin{aligned} \mathcal{M}_{cd}^{ab}(t, \tau) &= \langle a | [\hat{V}, \hat{V}_{cd}(t, \tau) - \hat{V}_{cd}(t, \tau)] | b \rangle \\ &= \langle a | \hat{V} \hat{V}_{cd}(t, \tau) | b \rangle - \langle a | \hat{V}_{cd}(t, \tau) \hat{V} | b \rangle - \langle a | \hat{V} \hat{V}_{cd}(t, \tau) | b \rangle + \langle a | \hat{V}_{cd}(t, \tau) \hat{V} | b \rangle. \end{aligned} \quad (\text{A21})$$

When the operator \hat{V}_{cd} acts on the vector $|b\rangle$, the only value of d that leads to non-zero results is $d = b$, so that $\hat{V}_{cd}(t, \tau) | b \rangle = \delta_{db} \hat{V}_{cb}(t, \tau) | b \rangle$, similarly in the expression $\langle a | \hat{V}_{cd}(t, \tau) = \delta_{ac} \langle a | \hat{V}_{ad}(t, \tau)$. Correspondingly, we have

$$\mathcal{M}_{cd}^{ab}(t, \tau) = \langle a | \hat{V} \hat{V}_{cb}(t, \tau) | b \rangle \delta_{bd} + \langle a | \hat{V}_{ad}(t, \tau) \hat{V} | b \rangle \delta_{ac} - \langle a | \hat{V}_{cd}(t, \tau) \hat{V} | b \rangle - \langle a | \hat{V} \hat{V}_{cd}(t, \tau) | b \rangle. \quad (\text{A22})$$

Using eqs. (A9), (A16) and (A18) we write a closed set of equations for all elements of the RDM $\rho_{ab}(t)$.

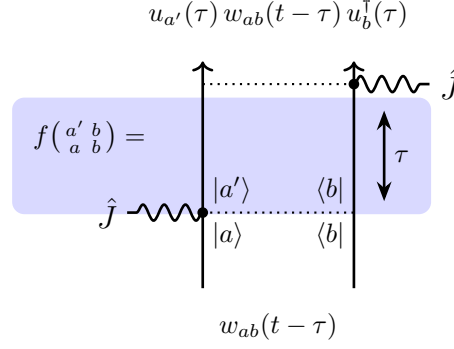


FIG. 1. Illustration of the bath evolution correlators, Eq. A18.

4. Full equation of motion for the RDM

The operators and superoperators defined above describe the evolution of the reduced density matrix $\hat{\rho}(t)$ exactly. The corresponding RDM equation

$$\frac{\partial}{\partial t} \hat{\rho}(t) = \hat{I}(t) - \mathcal{D}(t) \hat{\rho}(t) - \frac{i}{\hbar} [\hat{H}_S, \hat{\rho}(t)] - \sum_{cd} \int_0^t d\tau [\hat{V}, (\hat{V}_{cd}(t, \tau) - \hat{V}_{cd}(t, \tau))] \rho_{cd}(t - \tau). \quad (\text{A23})$$

This is an exact equation of motion for the RDM of an open quantum system with discrete levels. Its usage is only hindered by the need to evaluate Eqs. (A9), (A13) and (A18) which cannot be in general done exactly. Represented in the basis of eigenstates $|a\rangle$ of the Hamiltonian H_S we get

$$\frac{\partial}{\partial t} \rho_{ab}(t) = I_{ab}(t) - i\Omega_{ab}(t) \rho_{ab}(t) - \sum_{cd} \int_0^t d\tau \mathcal{M}_{cd}^{ab}(t, \tau) \rho_{cd}(t - \tau), \quad (\text{A24})$$

where $\omega_{ab} = \frac{\varepsilon_a - \varepsilon_b}{\hbar}$ are the transition frequencies between the eigenstates and all other terms are explicitly defined above.

5. Relaxation Rates

The particularly important case of the integral term is the contribution by which a diagonal element of the density matrix feeds into the change of another diagonal element. An integral term involving an integrand factor $\rho_{ab}(t - \tau)$ can be trivially time-localized by assuming $\rho_{ab}(t - \tau) \approx \rho_{ab}(t)$. We obtain time-dependent relaxation rates between electronic states:

$$K_{ab}(t) = 2\text{Re} \int_0^t d\tau \mathcal{M}_{bb}^{aa}(t, \tau) = \frac{2|J_{ab}|^2}{\hbar^2} \text{Re} \int_0^t d\tau e^{-g_{aa}(\tau) - g_{bb}(\tau) + 2\text{Im}[g_{bb}(t-\tau) - g_{bb}(t)] - i\omega_{ab}\tau} \quad (\text{A25})$$

These rates become the standard Förster resonance energy transfer rates upon the limit $t \rightarrow \infty$.

B: Bath correlation functions and lineshape functions

In this work, we assume a very simple model of the bath characterized by the Drude-Lorentz spectral density

$$J(\omega) = \frac{2\lambda\gamma\omega}{\omega^2 + \gamma^2} \quad (\text{B1})$$

with bandwidth γ and interaction strength λ . This leads to the two-point energy gap correlation function in the form [1]

$$\begin{aligned} C_{aa}(t) &= \text{tr}_B \{ U_g^\dagger(t) \hat{X}_a U_g(t) \hat{X}_a \hat{w}_{eq} \} = \\ &= \frac{\lambda_a}{\tau_a} \left(\cot \frac{\beta \hbar}{2\tau_a} - i \right) e^{-t/\tau_a} + \frac{4\lambda_a}{\beta \hbar \tau_a} \sum_{k=1}^{\infty} \frac{\nu_k}{\nu_k^2 - \tau_a^{-2}} e^{-\nu_k t}, \quad t \geq 0, \end{aligned} \quad (\text{B2})$$

where λ_a is the bath reorganization energy at site a and $\tau_a = \frac{1}{\gamma_a}$ the bath correlation time at site a . The corresponding lineshape function and its derivative read

$$g_{aa}(t) = \frac{1}{\hbar^2} \int_0^t d\tau \int_0^\tau d\tau' C_{aa}(\tau') = \frac{2}{\pi \hbar} \int_0^t d\tau \int_0^\tau d\tau' \int_{-\infty}^{\infty} d\omega J_a(\omega) \left(\coth \frac{\beta \hbar \omega}{2} \cos(\omega \tau') - i \sin(\omega \tau') \right), \quad (\text{B3})$$

$$\dot{g}_{aa}(t) = \frac{1}{\hbar^2} \int_0^t d\tau C_{aa}(\tau). \quad (\text{B4})$$

In numerical simulations, the correlation functions and the lineshape functions are obtained by applying the Padé expansion to the temperature-dependent part so that the whole correlation function can be approximated by $C_{aa}(\tau) \approx \sum_{k=0}^K c_{a,k} e^{-\gamma_k \tau}$. In our computations, we truncate at $K = 1$ as this proves sufficient given the smoothness of the Drude-Lorentz spectral density, in the numerical results this is computed using the `DrudeLorentzPadeBath()` function of Qutip [2] with `Nk = K = 1`.

C: Numerical integration of integro-differential equation

To calculate the evolution of the system, we treat Eq. (2) of the main text numerically by step-wise integrating both sides with a time step Δt . Using the Euler method, we arrive at an explicit expression for the evolution. Rearranged by common factors of $\rho(\cdot)$ we find

$$\begin{aligned} \rho(t + \Delta t) - \rho(t) &= \rho(0) \left[\frac{I(t + \Delta t) + I(t)}{2} \Delta t + \frac{\mathcal{M}(t, 0) + \mathcal{M}(t + \Delta t, 0)}{4} \Delta t^2 \right] + \\ &+ \rho(t) \left[\frac{\mathcal{L}(t)}{2} \Delta t + \frac{\mathcal{M}(t + \Delta t, t)}{2} \Delta t + \frac{\mathcal{M}(t, t)}{4} \Delta t^2 \right] + \\ &+ \rho(t + \Delta t) \left[\frac{\mathcal{L}(t + \Delta t)}{2} \Delta t + \frac{\mathcal{M}(t + \Delta t, t + \Delta t)}{4} \Delta t^2 \right] + \\ &+ \sum_{i=1}^{N_t-1} \rho(i\Delta t) \left[\frac{\mathcal{M}(t, i\Delta t) + \mathcal{M}(t + \Delta t, i\Delta t)}{2} \right] \Delta t^2. \end{aligned} \quad (\text{C1})$$

Here, $N_t = (t + \Delta t)/\Delta t$ refers to the number of time steps from 0 to the new time $t + \Delta t$. The stability of the integration method is guaranteed by comparison with the results from HEOM.

D: The Influence of Time Non-Local Effects

We study two versions of the the gFT theory, namely, the full time non-local one, and the time-localized version where for the population of the state $|a\rangle$ we replace $\rho_{aa}(t - \tau)$ is replaced with $\rho_{aa}(t)$. We compare two example dynamics in Fig. 2. In Fig. 2a, where $J < \lambda$ we notice that the initial population dynamics is much better captured by the time non-local gFT, while at long times the two versions of the gFT theory converge to each other, both deviating similarly from the results of HEOM. With larger coupling J , but HEOM and gFT predict oscillatory dynamics and a much slower equilibrium time than time-localized gFT. Time localized theory deviates from HEOM much earlier than the full time non-local theory. We can also see that the lasting oscillations on the population dynamics are only captured by the time non-local theory.

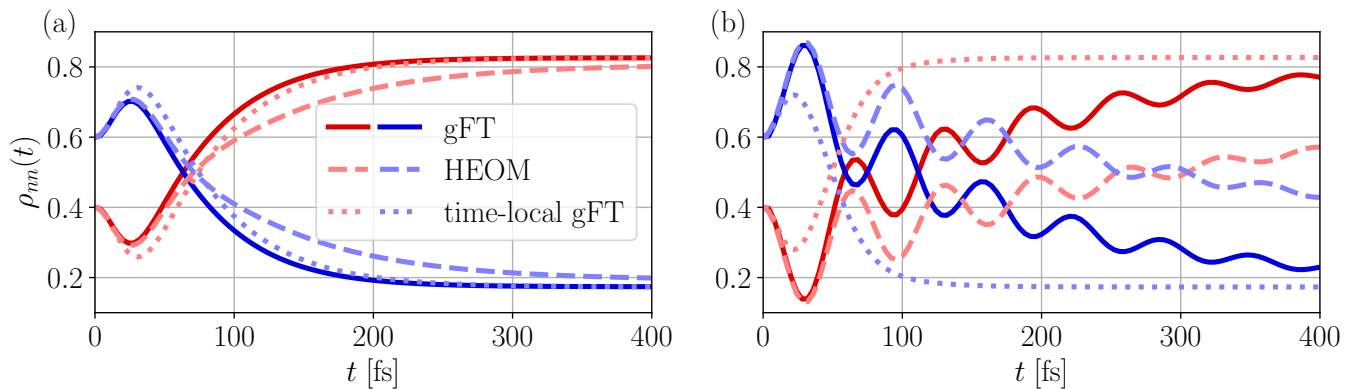


FIG. 2. Population evolutions comparing gFT, HEOM and the time localized version of gFT. For all calculations, $\Delta E = 300 \text{ cm}^{-1}$, $t_c = 30 \text{ fs}$ and $T = 277 \text{ cm}^{-1}$. In (a) $J = 110 \text{ cm}^{-1}$, $\lambda = 175 \text{ cm}^{-1}$. In (b) $J = 200 \text{ cm}^{-1}$, $\lambda = 175 \text{ cm}^{-1}$.

E: Comparison with Numerically Exact Propagation

In this section, we complement the parameter values shown in the main text with additional values of ΔE and more examples of evolutions. Due to the restriction to the single excitation of the dimer, the density matrix of the dimer is effectively that of a two level system and can thus be represented in the Bloch representation $\hat{\rho} = \frac{1}{2}(\hat{1} + x\hat{\sigma}_x + y\hat{\sigma}_y + z\hat{\sigma}_z)$, where the coordinates x, y encode the real and imaginary part of the coherence, respectively, and z encodes the population imbalance between the two sites. The trace distance between two density matrices has a very simple representation in the Bloch representation

$$T(\hat{\rho}, \hat{\rho}') = \sqrt{(x - x')^2 + (y - y')^2 + (z - z')^2}. \quad (\text{E1})$$

The error characterizes the maximum distance between two evolutions. One of the evolutions will be the reference numerical exact dynamics generated by HEOM, and the other evolution will be either the generalized Förster theory (gFT) developed in this work or the non-equilibrium version of the Förster theory (non-eq. FT). We consider errors for the populations and the coherences individually by splitting the contributions of the trace distance into the population part ε_{pop} and the coherence part ε_{coh} . With this we aim to better highlight the accuracy of the presented formalism. Since gFT cannot reproduce steady state delocalization due to the restriction to the site basis, we expect the error in populations to be much less than that of the coherences. We also differentiate between short and intermediate times. This leads us to define our error measures as

$$\varepsilon_{pop}^{\text{short}} = \max_{t \in [0, t_c]} |z^{\text{HEOM}}(t) - z^{\text{gFT}}(t)|, \quad (\text{E2a})$$

$$\varepsilon_{pop}^{\text{inter}} = \max_{t \in [t_c, t_s]} |z^{\text{HEOM}}(t) - z^{\text{gFT}}(t)|, \quad (\text{E2b})$$

$$\varepsilon_{coh}^{\text{short}} = \max_{t \in [0, t_c]} \sqrt{(x^{\text{HEOM}}(t) - x^{\text{gFT}}(t))^2 + (y^{\text{HEOM}}(t) - y^{\text{gFT}}(t))^2}, \quad (\text{E2c})$$

$$\varepsilon_{coh}^{\text{inter}} = \max_{t \in [t_c, t_s]} \sqrt{(x^{\text{HEOM}}(t) - x^{\text{gFT}}(t))^2 + (y^{\text{HEOM}}(t) - y^{\text{gFT}}(t))^2}. \quad (\text{E2d})$$

We hereby use the correlation time t_c to define the end of *short* times. The *intermediate* time is then taken from t_c until the steady state time t_s . This time is determined by setting a threshold on the rate of change of populations at advanced times (in cases where no steady state is reached, the simulation time is taken instead).

For consistency throughout the main text and in the SI we restrict ourselves to displaying the regimes of low errors between $\varepsilon \in [0, 0.1]$, since those highlight where the theories are valid. We consider $\varepsilon > 0.1$ as cases where the theory does not closely describe the real dynamics and we therefore do not discuss them in detail.

1. Molecules on resonance $\Delta E = 0$

Figures 3 and 4 show the error phase diagram as well as example evolutions of population dynamics in the degenerate case $\Delta E = 0$. The first significant point of these evolutions is that the two populations will converge to the equilibrium

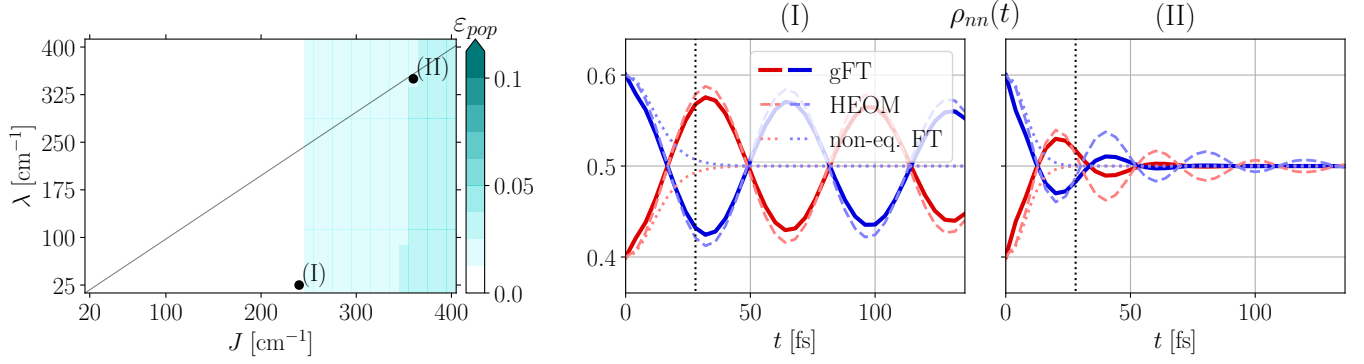


FIG. 3. Population-only trace distance comparing gFT and HEOM at short times and $\Delta E = 0$ with example evolutions showing the whole population dynamics.

value given by a uniform distribution between the two levels $\lim_{t \rightarrow \infty} \rho_{ii} = \frac{1}{2}$. The phase diagram in Fig. 3 shows that the short time evolution modeled by gFT follows that of HEOM very closely. Indeed, the maximum value of the error in the phase diagram is $\max_{\lambda, J} \varepsilon_{pop} < 0.04$. We also see that while the error depends on the hopping J , it does not depend on the reorganization energy λ . The reason for this is clear, the gFT predicts very correct behavior in short time intervals, especially due to the presence of the inhomogeneous term $\hat{I}(t)$. In particular, this makes the short time error show barely any dependence on λ .

In evolution (I), we observe oscillatory behavior for weak system bath coupling λ and moderate hopping J . This evolution shows many oscillations, and we do not see the times for which it stabilizes to the steady state. Note that for this case, non-eq. FT (dotted lines) predicts a very fast decay to the equilibrium value. This shows that our gFT works at short times in a regime where the Förster theory was not even expected to work (weak system-bath coupling).

Evolution (II) shows the evolution for strong system-bath coupling λ and strong hopping J . This is another example of a case where Förster theories are not guaranteed to work. However, we see that at short times gFT closely reproduces the HEOM damped oscillations, with an error slightly higher than the one in the previous evolution. In comparison, non-eq. FT again fails to model these oscillations and predicts monotonous convergence to the steady state. For longer times, we see that the gFT slightly underestimates the following bumps in the oscillation.

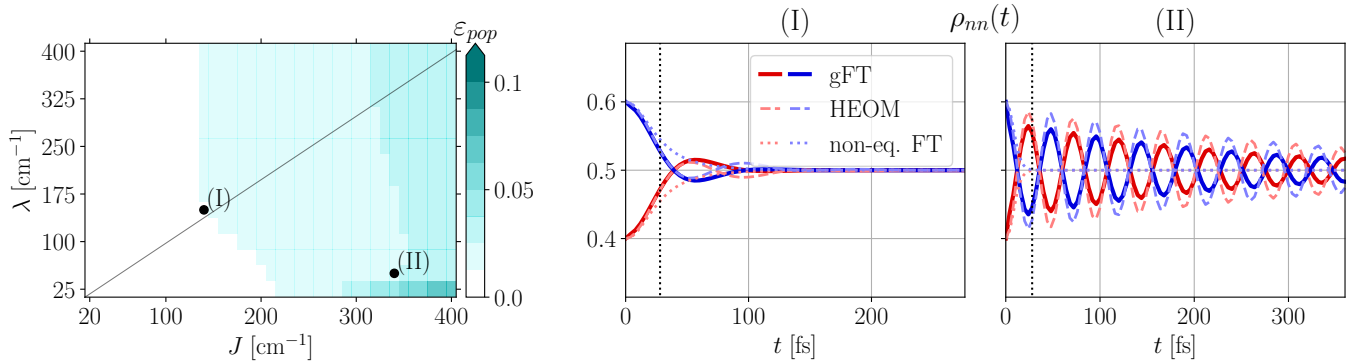


FIG. 4. Population-only trace distance comparing gFT and HEOM at intermediate times and $\Delta E = 0$ with example evolutions showing the whole population dynamics. Although hard to see, the dotted line non-eq. FT result quickly converges to 0.5.

Figure 4 shows that gFT also provides a good model for intermediate times. In the phase diagram we observe that ε_{pop} remains quite small $\varepsilon \approx 0.03$. Comparing with the short time error phase diagram in the previous figure we now see a more nontrivial dependence with the parameters. In particular, for smaller values of J we have an error $\varepsilon_{pop} < 0.02$. Interestingly, the boundary of this region does not depend on λ for $\lambda > J$. For $\lambda < J$ we see that the error increases with a stronger system-bath coupling. This is quite counter-intuitive, as the opposite (i.e. larger error at stronger system-bath coupling) is expected. Evolution (I) shows an example dynamics where gFT closely reproduces the damped oscillations of HEOM, while non-eq. FT predicts monotonous decay. Evolution (II), in the weak system bath coupling regime, shows that gFT models the HEOM evolution with reasonable accuracy, even out

of its regime of applicability for intermediate times. In particular we see that the dynamics has some fast oscillations that slowly decay towards equilibrium. gFT also predicts those oscillations, only with slightly smaller peaks. Close inspection shows that non-equ. FT theory (dotted line) completely misses the damped oscillations.

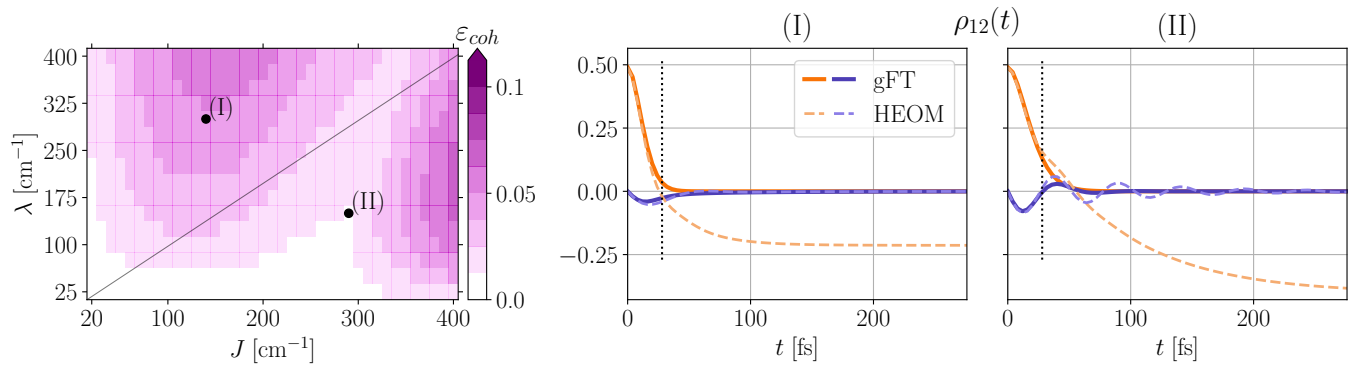


FIG. 5. Phase diagram (left) for the short time difference of coherences ε_{coh} between generalized Förster Theory and HEOM for degenerate levels $\Delta E = 0 \text{ cm}^{-1}$. Plots (I) and (II) depict two example time evolution comparing gFT (solid) and HEOM (dashed). Evolution (I) is taken in the blob at strong system bath coupling, and evolution (II) is chosen at the intersection of the two blobs in the weak system-bath coupling regime.

Figure 5 shows the error in the coherences ε_{coh} at short times. We see that, as expected, gFT does not provide a good theory for the coherences for short times. Nonetheless, the error remains contained at short times $\varepsilon_{coh} < 0.08$. Interestingly, the region with small error at short times does not agree with the expected strong system-bath coupling regime of applicability $\lambda > J$. Indeed we observe that there is a region at small λ where the error remains very small. The evolution (II) illustrates this region, where we see exactly that, although at long times the coherence saturates to a large negative value. This clearly cannot be captured by gFT due to the choice of the site basis. However, for short times $t < t_c$ we see that the gFT evolution remains very close to HEOM. It is also interesting to note that, in this region, HEOM predicts oscillatory behavior of the imaginary part, while gFT does not capture this feature. The phase diagram shows that there are two regions with larger error, corresponding to very large λ and very large J . Evolution (I) illustrates the dynamics in one of these regions. We see that the gFT evolution starts deviating from HEOM already at $t < t_c$. At long times the coherence is non-zero in HEOM, but, interestingly, it is smaller than that of evolution (II). This shows that the short time validity of gFT cannot be inferred from the long-time results, and thus gFT at short times is not only valid for strong system bath coupling. Indeed, the region with smaller error occurs at small λ .

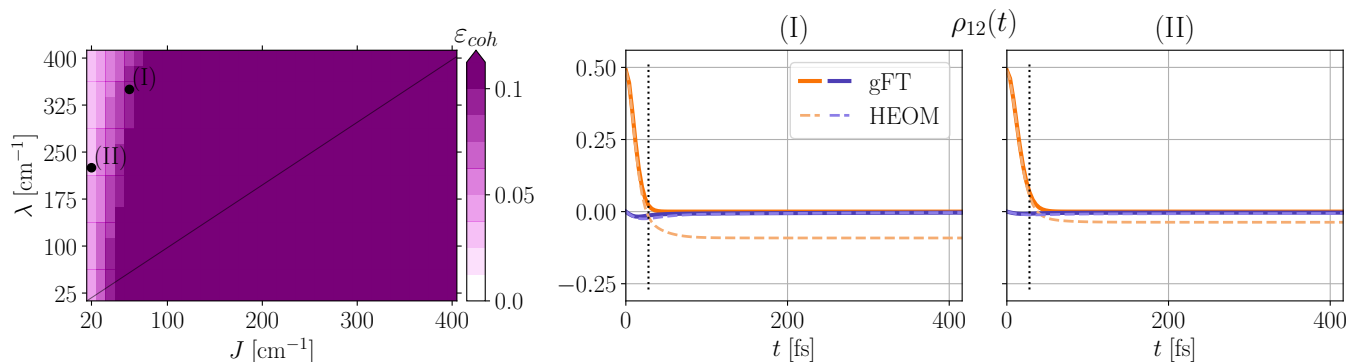


FIG. 6. Phase diagram (left) for the intermediate time difference of coherences ε_{coh} between generalized Förster Theory and HEOM for degenerate levels $\Delta E = 0 \text{ cm}^{-1}$. Plots (I) and (II) depict two example time evolution comparing gFT (solid) and HEOM (dashed). Both of these evolutions are chosen at extremely weak hopping J , where the delocalization in the site basis is very small. They depict a case where gFT is still quite accurate (II) and a case with larger error $\varepsilon_{coh} \approx 0.1$ (I).

Figure 6 shows the long-time error of the coherence. As expected and already discussed, gFT cannot model long time coherence in the site basis. For this reason, we see that the error is large $\varepsilon > 0.1$ almost in the phase diagram. The only region where the error is $\varepsilon < 0.1$ is for very small J , where the delocalization in the site basis will be very

small. An example of this is evolution (II) where we see that the coherence saturates to a non-zero, but small value. The example evolution (I) is close to $\varepsilon_{coh} = 0.1$, and thus serves as an illustration for what a trace distance of $\varepsilon \approx 0.1$ physically represents, thus justifying our choice not to show these evolutions and focus on the ones where gFT is a good model.

2. Intermediate energy difference $\Delta E = 50$

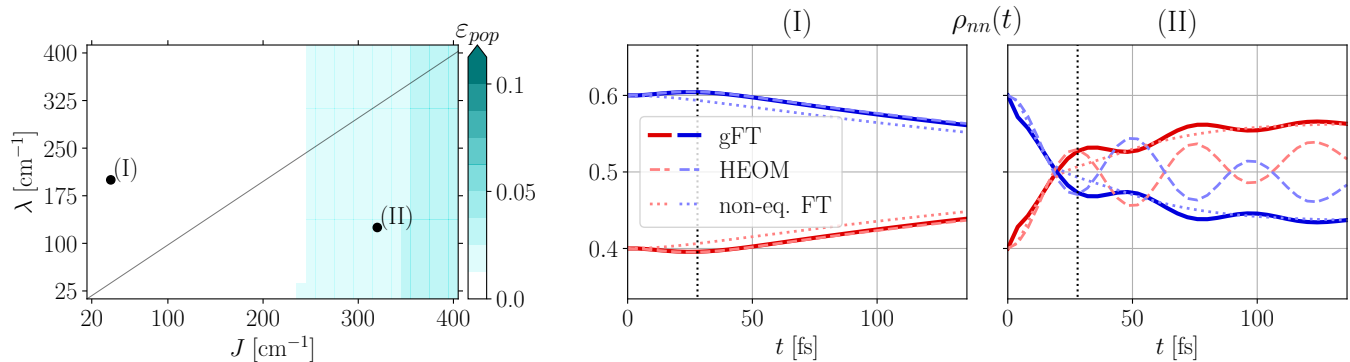


FIG. 7. Phase diagram for the short time population error between gFT and HEOM (left) for $\Delta E = 50 \text{ cm}^{-1}$ (same as in Fig 1 of main text). Evolution (I) shows an example where the short time error is very small $\varepsilon_{pop} < 0.0125$, note that non-eq. FT already deviates from HEOM at short times. Evolution (II) shows a case at weak system-bath coupling, where the error is a bit larger, but gFT still remains relatively close to HEOM at short times.

Figure 7 shows the error phase diagram for an intermediate energy difference between the two dimers of $\Delta E = 50$. The behavior is fairly similar to the one observed in Fig. 3, with a very small error at short times $\varepsilon_{pop} < 0.04$. The two example evolutions display the difference at short times, highlighting a very accurate evolution (I) with a very small error. Although non-eq. FT also works well in this regime, we see that gFT is closer to HEOM. Evolution (II) shows an evolution where the short time error is larger, and indeed we see that HEOM and gFT show a small deviations.

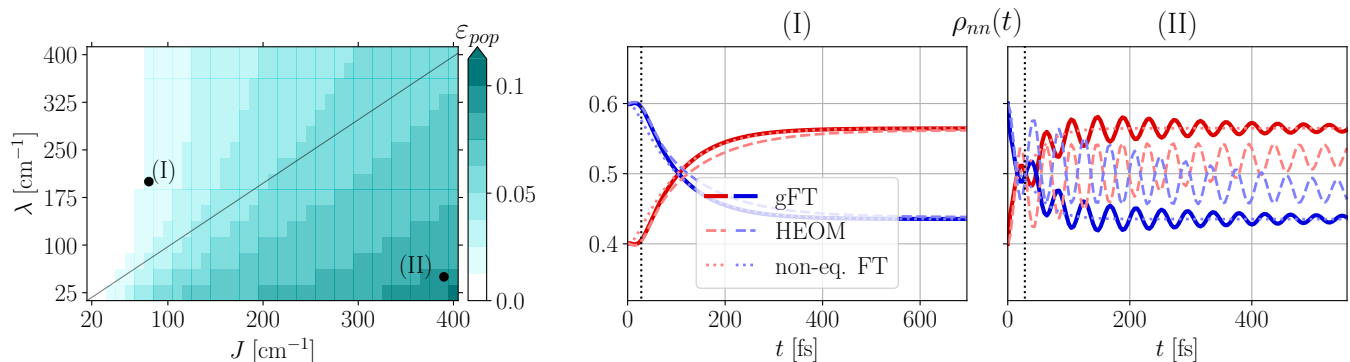


FIG. 8. Phase diagram for the intermediate time population error ε_{pop} (left) between gFT and HEOM for $\Delta E = 50 \text{ cm}^{-1}$ (same as in main text). Note that at intermediate times the validity of gFT aligns with the usual strong system-bath coupling regime. Evolution (I) depicts a case where the error is very small $0.0125 < \varepsilon_{pop} < 0.025$ and we see that this error happens around $t \approx 200 \text{ fs}$ where the population of HEOM grows more slowly towards the steady state. Evolution (II) shows a case with larger error $\varepsilon_{pop} \approx 0.1$ arising at very weak system-bath coupling. In this we see that gFT oscillates around a different value than HEOM since gFT converges to canonical equilibrium in the site basis.

Figure 8 shows the error of the population at intermediate times. This phase diagram clearly shows that gFT is valid for strong system bath coupling $\lambda > J$. However, we see that the boundaries of the regions with similar error do not seem to be simple linear functions of J . This suggests that the gFT is valid when $\lambda > f(J)$, where $f(J)$ is a nonlinear function, which will generally depend on the rest of the parameters ΔE , $k_B T$, t_c . We see however, that

gFT is valid for quite a wide range of parameters. As stated in the main text, it should be noted that gFT has smaller error at *intermediate* times than non-eq. FT at *short* times. Evolution (I) shows an example where gFT captures the HEOM dynamics well, with only small deviations for $100 \text{ fs} \lesssim t \lesssim 300 \text{ fs}$. Non-eq. FT shows a deviation from HEOM and gFT at short times, but then agrees perfectly with gFT. The reason for this is simply that the parameters are in the regime of applicability of Förster $\lambda > J$. Evolution (II) shows a case where the error is larger $0.075 < \varepsilon_{coh} < 0.1$. In this case we see that gFT predicts some of the oscillatory behavior of HEOM. Although the frequency of the oscillations is reasonably well captured by gFT, the value around which they oscillate is not the same as in HEOM. This could be caused by the fact that gFT always predicts an equilibrium state in the site basis, so the populations saturate to $1/(1 + e^{\pm\beta\Delta E})$, while HEOM can account for equilibrium in a different basis $\rho = e^{-\beta H'}/Z_\beta$. In comparison, we see that non-eq. FT does not predict oscillations, but saturates to the same equilibrium value as gFT.

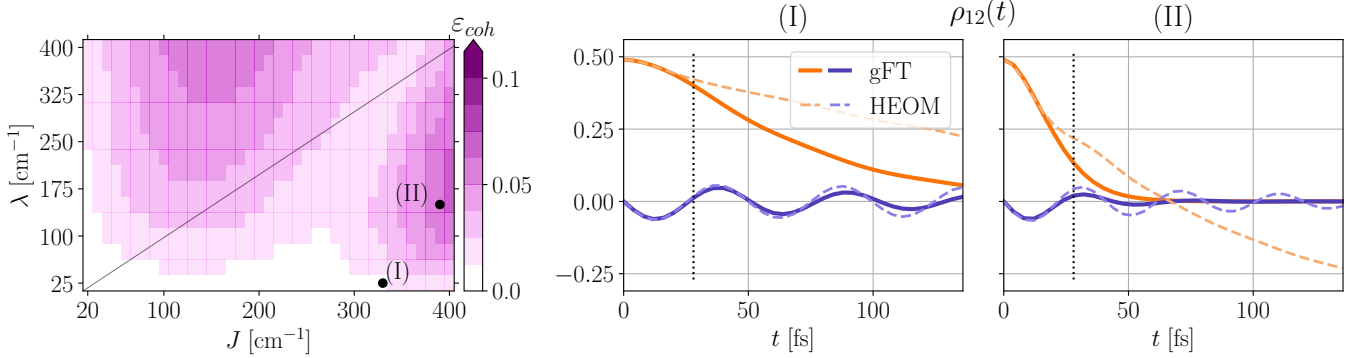


FIG. 9. Phase diagram (left) for the short time difference of coherences ε_{coh} between gFT and HEOM for $\Delta E = 50 \text{ cm}^{-1}$. Plots (I) and (II) depict two example time evolution comparing gFT (solid) and HEOM (dashed). Evolution (I) is taken in the region of small error at weak system system bath coupling, where we see gFT and HEOM agreeing quite well until $t = t_c$. Evolution (II) is chosen in the blob of weak system-bath coupling, where we see a larger deviation of HEOM from gFT, specially on their real part.

Figure 9 shows the error in the coherences at short times for $\Delta E = 50$. The phase diagram is quite similar to Fig. 5 showing two regions of high error for large λ and for large J , and a low error region at small λ . Evolution (I) illustrates the behavior in this low error region, we see that the real part of the coherence for gFT closely follows HEOM until they depart right before t_c . Interestingly, the evolution of the imaginary part is accurate for longer, capturing the oscillations. This is not the case for (II) where we see a big departure of the HEOM coherence from the gFT, also for the imaginary part.

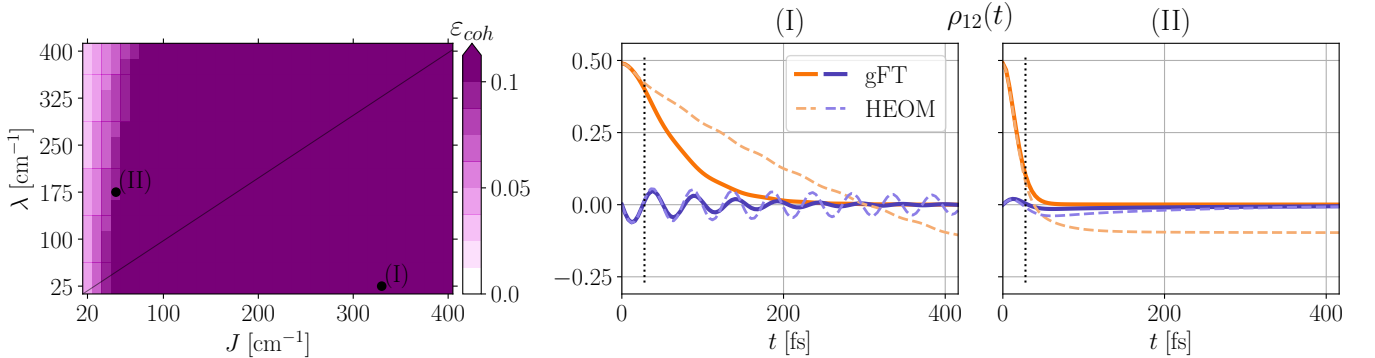


FIG. 10. Phase diagram (left) for the intermediate time difference of coherences ε_{coh} between gFT and HEOM for $\Delta E = 50 \text{ cm}^{-1}$. Evolution (I) is the same as in Fig. 9. Evolution (II) shows an error of $\varepsilon_{coh} \approx 0.1$.

Figure 10 shows that at intermediate times, the coherence dynamics predicted by gFT are completely different from those of HEOM, as we expected. Evolution (I) is the same as in Fig. 9 and we see that HEOM shows long lived oscillations of the imaginary part, which die out in gFT, and the real part does not agree at all between the two cases. On the contrary, evolution (II), although it also has a considerable error, shows that this error comes mostly from the

saturation value of the real part of the coherence due to delocalization.

3. Large energy difference $\Delta E = 300$

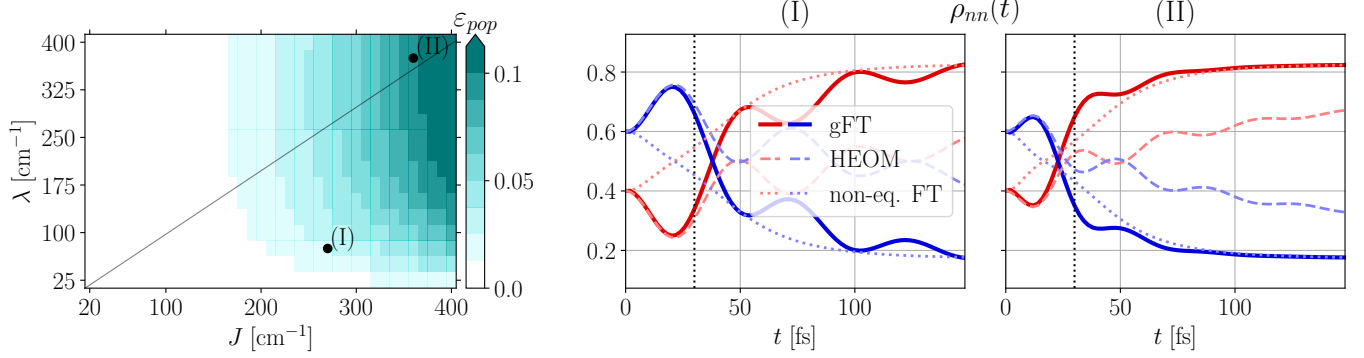


FIG. 11. Phase diagram for the short time population error ε_{pop} between gFT and HEOM (left) for $\Delta E = 300 \text{ cm}^{-1}$. Evolution (I) shows an example at weak system-bath coupling with very small error $\varepsilon_{pop} \approx 0.025$ with large error from non-eq. FT. Evolution (II) shows a case with larger error $\varepsilon_{pop} \approx 0.1$ where gFT and HEOM deviate after the first bump.

Figure 11 shows the population error at short times for a large energy difference between the two energies of the dimer. We observe that in this case, even the short time error can be large, with some values $\varepsilon_{pop} > 0.1$ for very strong J and strong λ . The phase diagram also illustrates how the region with small $J < 150$ has very small short time error and how the region with very small $\lambda \approx 25$ also has small error. This confirms, once more, that the short time validity of gFT is not restricted to strong system-bath coupling. Evolution (I) shows a case where the short time error is small ε_{pop} . It shows a distinctive feature of the large ΔE case, the presence of a peak at short times, which arises due to the inhomogeneous term $\hat{I}(t)$ and thus cannot be captured by non-eq. FT. We therefore see that gFT captures the initial peak, describing much better the short time behavior of HEOM. At longer times, as we already saw before, gFT shows some oscillations, which are also shown by HEOM, but which are not at the same values of the population. In this case non-eq. FT performs very poorly and does not approximate the HEOM evolution at any time. Evolution (II) is an example that even modelling the initial peak well does not guarantee that the short time evolution will be well described, since we see the two evolutions separating already before t_c .

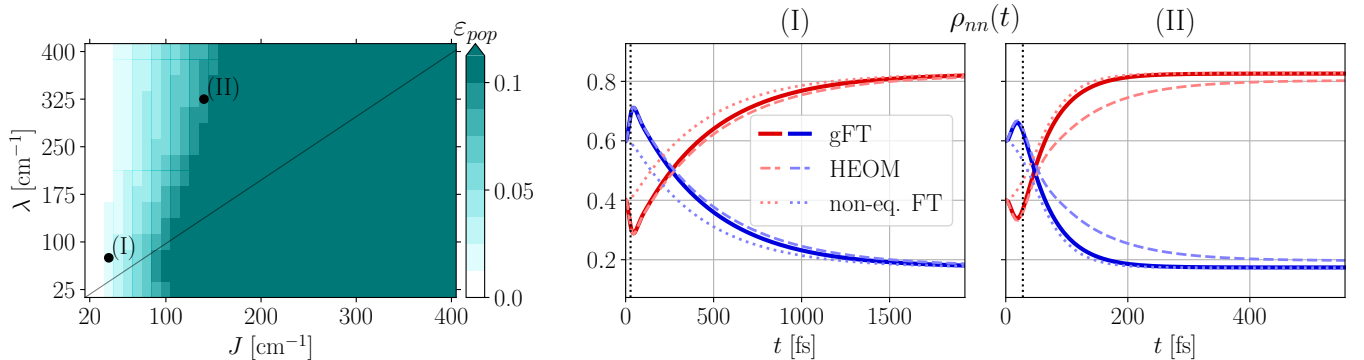


FIG. 12. Phase diagram for the intermediate time population error ε_{pop} between gFT and HEOM (left) for $\Delta E = 300 \text{ cm}^{-1}$. Evolution (I) shows a case with low error, which non-eq. FT fails to model accurately. Evolution (II) shows a case with larger error $\varepsilon_{pop} \approx 0.1$ where again HEOM shows a slower relaxation towards equilibrium than Förster theories.

Figure 12 shows the population error at intermediate times for large ΔE . We see that in this limit, a large part of the phase diagram has large error $\varepsilon_{pop} > 0.1$. This suggests that the validity of gFT for intermediate times critically depends on ΔE . As expected the regime of validity of the theory is for strong system bath coupling $\lambda > J$. Evolution (I) shows an example where the presence of the short time peak separates the predictions of gFT and non-eq. FT so

that only gFT provides a good model for the HEOM evolution. However, in evolution (II) we see an example where HEOM deviates from gFT after the populations cross.

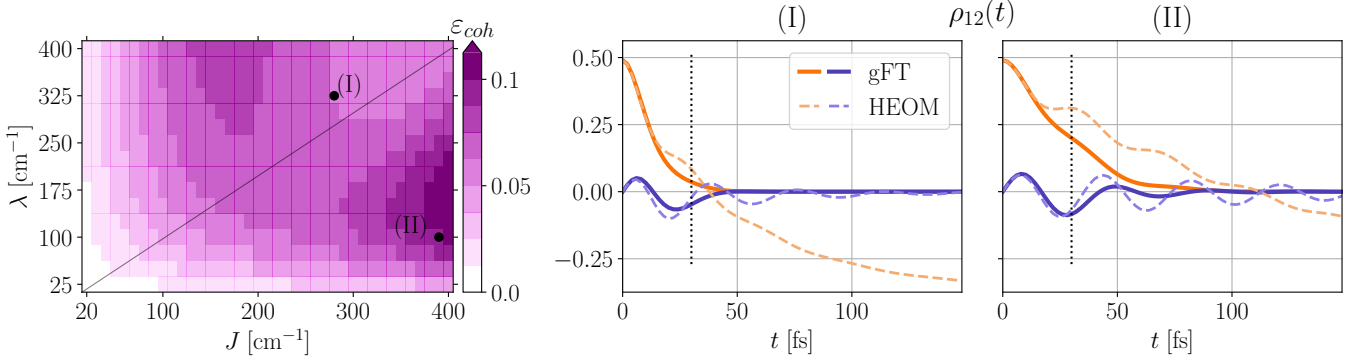


FIG. 13. Phase diagram (left) for the short time difference of coherences ε_{coh} between gFT and HEOM for $\Delta E = 300 \text{ cm}^{-1}$. Evolution (I) shows an example with moderate error in between the two blobs, and evolution (II) shows an example with large error in the weak system-bath coupling blob. We again see that most of the error comes from the real part of the coherence.

Figure 13 shows that for large ΔE , the region where the short time coherence is well captured moves to the lower left corner of the phase diagram with small λ and J . The phase diagram still retains two lobes with a high error, although now the large J has a higher error value. Evolution (I) illustrates the deviations at short times for large J and large λ , while evolution (II) shows that the real part of the coherence acquires some oscillatory behavior, which therefore gives a larger error at short times.

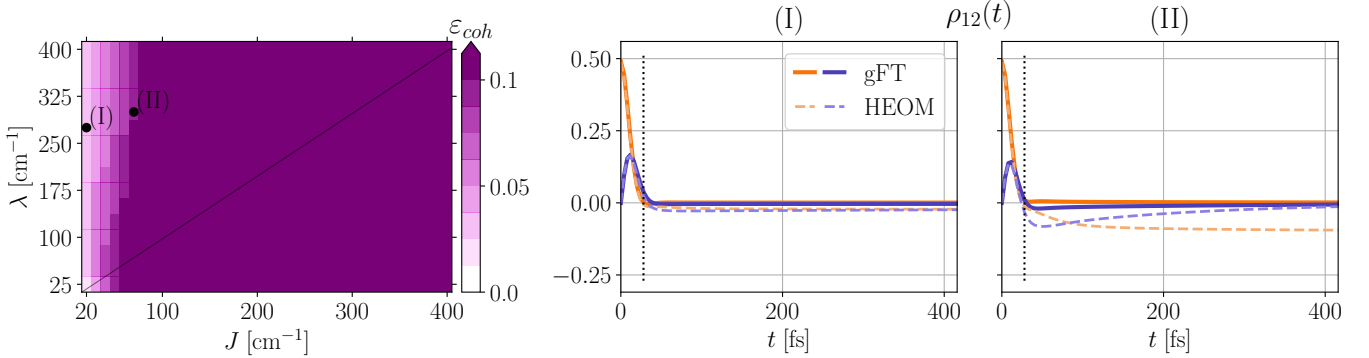


FIG. 14. Phase diagram (left) for the intermediate time difference of coherences ε_{coh} between gFT and HEOM for $\Delta E = 300 \text{ cm}^{-1}$. Evolution (I) shows an example at very small J where the error is small, and evolution (II) an example with larger error $\varepsilon_{pop} \approx 0.1$.

Lastly, Fig 14 shows a similar behavior for the intermediate time coherence error to the other values of ΔE . Only systems with very small J have a relatively small intermediate time coherence error. Evolutions (I) and (II) represent two examples of the low error region and at the boundary, respectively.

-
- [1] S. Mukamel, *Principles of Nonlinear Spectroscopy* (Oxford University Press, Oxford, 1995).
 [2] N. Lambert, E. Giguère, P. Menczel, B. Li, P. Hopf, G. Suárez, M. Gali, J. Lishman, R. Gadhvi, R. Agarwal, A. Galicia, N. Shammah, P. Nation, J. Johansson, S. Ahmed, S. Cross, A. Pitchford, and F. Nori, Qutip 5: The quantum toolbox in python, *Physics Reports* **1153**, 1 (2026).